npj computational materials

www.nature.com/npjcompumats

ARTICLE OPEN

Check for updates

Enhancing ferromagnetic coupling in CrXY (X = O, S, Se; Y = Cl, Br, I) monolayers by turning the covalent character of Cr-X bonds

Hao-Ran Zhu[1], Bin Shao[1,2]✉ and Xu Zuo[1,3,4]✉

On the basis of first-principles calculations, we investigate the electronic and magnetic properties of 1T phase chromium sulfide halide CrXY (X = O, S, Se; Y = Cl, Br, I) monolayers in $CrCl_2$ structure with the $P\bar{3}m1$ space group. Except for the CrOI monolayer, all CrXY monolayers are stable and ferromagnetic semiconductors. Our results show that the ferromagnetic coupling is dominated by the kinetic exchange between the empty e_g-orbital of Cr atoms and the *p*-orbital of anions under the three-fold rotational symmetry. In this context, the coupling strength allows for being greatly enhanced by turning the nature of Cr–X bonds, i.e., increasing the covalent contribution of the bonds by minimizing the energy difference of the coupled orbitals. As we illustrate for the example of CrOY, the Curie temperature (T_c) is nearly tripled by substituting O by S/Se ion, eventually reaching the highest T_c in CrSeI monolayer (334 K). The high stabilities and Curie temperature manifest these monolayer ferromagnetic materials feasible for synthesis and applicable to 2D spintronic devices.

npj Computational Materials (2023)9:56 ; https://doi.org/10.1038/s41524-023-01013-8

INTRODUCTION

The discovery of monolayer magnetic material CrI_3[1] opens the door to the development of two-dimensional (2D) spintronic devices aiming for ultralow energy consumption, ultrafast device operation, and ultrahigh density information storage[2–4]. For practical applications, it is highly desired to enhance the strength of magnetic exchange interaction such that the magnetic device can be operated at room temperature (300 K). However, up to now, the Curie temperatures of 2D ferromagnetic semiconductors reported in experiments are much lower than room temperature, e.g., the T_c of CrI_3 and $CrGeTe_3$ are 45 K[1] and 20 K[5], respectively. Thus, it remains a challenging task of searching 2D ferromagnetic semiconductors with high T_c[6–10].

Generally, the magnetic cations in transition-metal semiconductors are separated by nonmagnetic anions. Magnetic couplings mainly involve kinetic exchange mechanism, or the so-called superexchange interaction, i.e., the magnetic exchange of *d*-electron-bearing cations arises from virtual hopping between the cation *d*-orbital and anion *p*-orbital. In crystals, the symmetry properties not only determine whether the virtual hopping is allowed, but also decide the sign of magnetic exchange interaction, i.e., being of ferromagnetic (FM) or antiferromagnetic (AFM) exchange[11–13]. According to the Goodenough–Kanamori–Anderson rule, when the interacting cation–anion–cation path makes an angle of 90°, the magnetic coupling of cations prefers FM exchange[11,14,15]. Besides, the strength of this virtual hopping is related to the covalent admixture amplitude of *p*–*d* bonds from perturbation theory $\langle p|\boldsymbol{H}_{\mathrm{crystal}}|d\rangle/\Delta_{pd}$, where the Δ_{pd} is the energy difference of the *p*- and *d*-orbital level[16]. Thus, it suggests that the FM exchange interaction in semiconductors could be realized by carefully choosing the symmetry of the crystal field and its strength is associated with the admixture level of *p*- and *d*-orbital, i.e., the covalent character of *p*–*d* bonds.

In this work, based on first-principles calculations, we investigate a series of semiconducting ferromagnets, 1T phase chromium sulfide halide CrXY (X = O, S, Se; Y = Cl, Br, I) monolayer. Both the calculated phonon spectra and molecular dynamics (MD) simulations indicate that the CrXY monolayer is thermodynamically stable except for the CrOI monolayer. Given the nearly 90° Cr–X/Y–Cr interacting path and the three-fold rotational symmetry, the magnetic interaction between Cr ions favors FM exchange, which is confirmed by our energetic estimations of various magnetic configurations. Furthermore, our results show that the FM coupling is mainly contributed from the hybridization between the empty e_g-orbital of Cr atoms and the *p*-orbital of anions. Using a simple Hamiltonian model, we reveal a general mechanism that FM coupling in CrXY monolayers can be significantly enhanced by reducing the energy difference between *p*- and *d*-orbitals, especially for *p*- and e_g-orbitals. As a result, by minimizing the energy difference of the e_g- and *p*-orbital level, which is achieved by substituting O by S/Se, the covalent character of the hybridization is greatly enhanced, yielding the increasement of the T_c from 49 K to 334 K (CrSeI).

RESULTS AND DISCUSSION

Geometrical configuration and stabilities

The 1T phase chromium sulfide halide CrXY monolayer is constructed by substituting one of the chalcogen atom (X) by a halogen atom (Y) in one atomic layer of CrX_2, as shown in Fig. 1a. Each Cr atom is coordinated by three chalcogen atoms and three halogen atoms, resulting in a strongly distorted octahedron. The dynamic and thermal stabilities of the CrXY monolayer are studied by calculating phonon spectra and performing molecular

[1]College of Electronic Information and Optical Engineering, Nankai University, Tianjin, China. [2]Tianjin Key Laboratory of Optoelectronic Sensor and Sensing Network Technology, Nankai University, Tianjin, China. [3]Key Laboratory of Photoelectronic Thin Film Devices and Technology of Tianjin, Nankai University, Tianjin, China. [4]Engineering Research Center of Thin Film Optoelectronics Technology, Ministry of Education, Nankai University, Tianjin, China. ✉email: bshao@nankai.edu.cn; xzuo@nankai.edu.cn

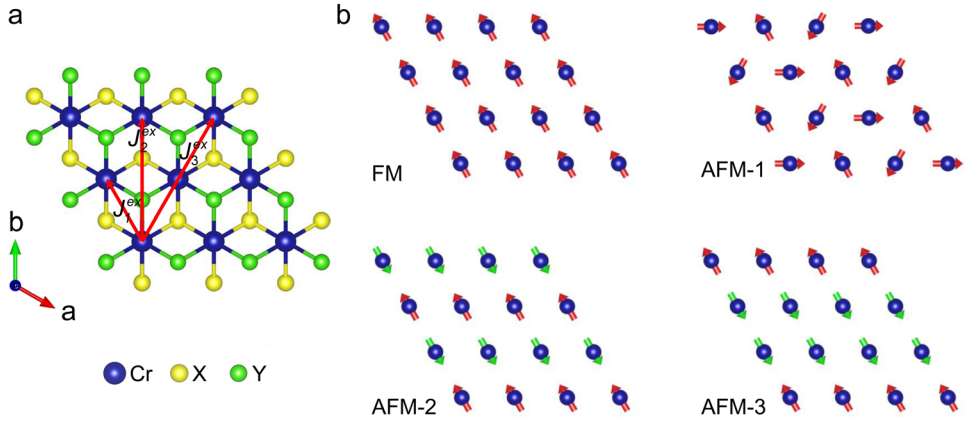

Fig. 1 Geometrical and magnetic configuration of CrXY monolayer. a 1T phase chromium sulfide halide CrXY monolayer crystal structure and the magnetic exchange paths. **b** Four different magnetic spin ordering configurations are involved. The blue, yellow and green balls represent the Cr atom, chalcogen atom (X) and halogen atom (Y), respectively.

Table 1. Energies of CrXY monolayers.

	FM	AFM-1	AFM-2	AFM-3
CrOCl	0	30.06	24.14	12.11
CrOBr	0	13.35	6.99	1.36
CrSCl	0	203.96	73.05	20.31
CrSBr	0	114.40	101.48	47.09
CrSI	0	106.22	93.38	43.45
CrSeCl	0	96.12	93.01	32.01
CrSeBr	0	110.20	103.74	40.29
CrSeI	0	119.30	109.61	46.14

Calculated relative energies (meV/Cr) for various magnetic configurations of CrXY monolayers, as shown in Fig. 1b. The FM state is chosen as energy reference.

dynamics (MD) simulations, respectively. In the calculated phonon spectra (Supplementary Fig. 1), no imaginary phonon mode is observed except for the CrOI monolayer, suggesting that the CrXY monolayers are dynamically stable. Hereafter, the CrOI monolayer will not be discussed in the following. To confirm the thermal stability, we perform MD simulations of the CrXY monolayers at 300 K for 20 ps. As revealed by MD snapshots (the inserts in Supplementary Fig. 2), the surface morphology is basically unchanged during the simulations, implying that those monolayers are thermally stable. Furthermore, we have investigated mechanical stability by calculating the elastic constants. Supplementary Table 1 shows that all CrXY monolayers satisfy the Born conditions[17] (C_{11}, C_{22}, and $C_{44} > 0$, and $C_{11}C_{22} - C_{21}^2 > 0$), suggesting that they are mechanically stable.

Magnetic ground state

To address the magnetic ground state of CrXY monolayers, we compare the energies of several typical magnetic configurations, including non-collinear magnetic structure (FM, AFM-1, AFM-2 and AFM-3, shown in Fig. 1b)[18]. Table 1 shows that the energy of FM state in each system is lower than the energies of all AFM states. The net magnetic moment of all 2D CrXY monolayers is about $3\mu_B$/f.u., indicating a d^3 electron configuration in high spin state. Furthermore, we calculate the total energy as a function of the magnetic propagation vector $\boldsymbol{q} = (q_x, q_y)$ by utilizing the generalized Bloch theorem (gBT)[19]. As shown in Fig. 2a and Supplementary Fig. 3, the minimum of the curve is located at $\boldsymbol{q} =$ (0, 0), indicating that the magnetic ground states of all 2D CrXY monolayers are FM state.

Figure 2b and Supplementary Fig. 4 show the calculated spin-dependent density of states (DOS) of the CrXY monolayers, with the coordinates based on the octahedron of CrX_3Y_3 (the inset of Fig. 2b). All CrXY monolayers are FM semiconductor, and Cr-3*d* orbitals split into the triplet orbitals t_{2g} and doublet orbitals e_g in the octahedral crystal field. Meanwhile, the lower t_{2g}-orbitals are half occupied, and the e_g-orbitals also have significant electron occupation, indicating a sizable interaction with the *p*-orbitals of the anion.

For realizing the long-range FM ordering in CrXY monolayers, the magnetic anisotropy is an essential prerequisite[20]. The magnetic anisotropy energy (MAE) is calculated by comparing different spin directions, the energies differences for different spin directions are shown in Supplementary Fig. 5. Except for CrSeCl and CrSeBr monolayers, the energies minimum of the spin direction are in the *x*–*y* plane, other CrXY monolayers are along the out-of-plane direction. All CrXY monolayers exhibit magnetic anisotropy, demonstrating that long-range FM ordering can emerge at certain temperatures.

Next, we calculate the magnetic exchange interaction parameters J^{ex} by means of the four-state method[21,22], which includes the first-nearest-neighbor (J_1^{ex}), second-nearest-neighbor (J_2^{ex}) and third-nearest-neighbor (J_3^{ex}) (Fig. 1a). As shown in Table 2, the J_1^{ex} is dominated and positive, which is crucial in determining the FM ordering. Besides, it is worth noting that when substituting O ion by S/Se ion the J_1^{ex} is greatly enhanced. (Other *U* choices of 1, 1.5, 2, and 2.5 eV are also presently tested and qualitatively render the same results, as shown in Supplementary Table 2)

Ferromagnetic superexchange mechanism

Given the angle of ∠Cr–X/Y–Cr being close to 90°, the superexchange interaction between Cr ions in CrXY monolayer prefers FM exchange[11,14,15]. Besides, because of the three-fold rotational symmetry, the three *p*-orbitals of anion are split into singlet orbital $(1/\sqrt{3})(p_x + p_y + p_z)$ defining as p_σ and doublet orbitals being of $(1/\sqrt{2})(p_x - p_y)$ and $(1/\sqrt{6})(p_z - p_x - p_y)$, the coordinates referring to the coordinate axes parallel to the lines connecting the anion to the three neighboring cations. The singlet orbital p_σ has a large overlap with the e_g-orbitals of the cations, i.e., there is a sizable hybridization between the p_σ- and e_g-orbitals of all three surrounding X/Y ions, which can be inferred from the wave function depicted in Supplementary Fig. 6a. For each pair of Cr-X/Y, this hybridization leads to exchange polarization. If the spins of the three cations are all parallel to each other (FM ordering), the

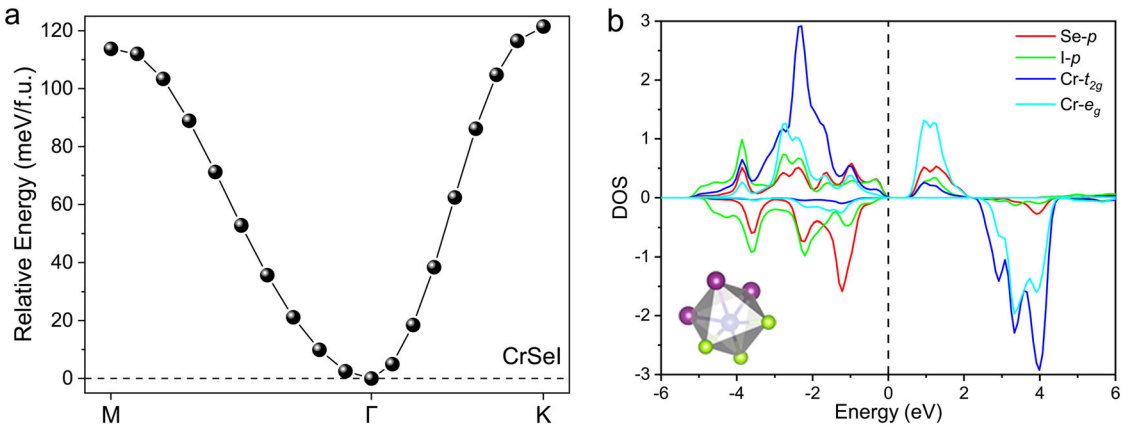

Fig. 2 Magnetic and electronic properties of CrSeI monolayer. a Energy dependence on the magnetic propagation vector ***q***, (**b**) density of state (DOS) of the CrSeI monolayer. The valence band maximum (VBM) energy is set to zero.

Table 2. Magnetic properties of CrXY monolayers.

	J_1^{ex}	J_2^{ex}	J_3^{ex}
CrOCl	3.11	0.06	0.05
CrOBr	1.43	0.05	0.08
CrSCl	11.64	0.37	−0.60
CrSBr	11.66	0.32	−0.47
CrSI	11.05	0.24	−0.46
CrSeCl	11.33	0.51	−1.63
CrSeBr	12.53	0.48	−1.33
CrSeI	13.12	0.41	−1.02

Calculated magnetic exchange interaction parameters J^{ex} (in meV) of CrXY monolayers, the magnetic exchange paths are shown in Fig. 1a.

energy due to the exchange polarization would be the lowest, since the singlet orbital p_σ overlaps them equally[15].

To interpret the enhanced J_1^{ex} when substituting O ion by S/Se ion, we consider a model to describe the superexchange interaction between two Cr ions via the anion in-between. For simplicity, this model involves one *p*-orbital of the anion, and two *d*-orbitals for each Cr ions, in which the lower orbital is half occupied and the higher one is empty referring to the t_{2g} and e_g orbitals, respectively. The Hamiltonian is given as:

$$\hat{H} = \hat{H}_M + \hat{H}_L + \hat{H}_U + \hat{H}_t\,, \tag{1}$$

where the first two terms $\hat{H}_M$ and $\hat{H}_L$ are the on-site energy terms for the transition metal and anion ligand, respectively, the third term $\hat{H}_U$, describes the Coulomb repulsion between two electrons in *d*-orbital (the repulsion between electrons in the *p*-orbital is neglected), the last term $\hat{H}_t$ represents the hybridization between *p*- and *d*-orbitals and reads

$$\hat{H}_t = \sum_{i=l,r}\sum_{\mu=\alpha,\beta}\sum_{\sigma=\uparrow,\downarrow} t_{p\mu}(c^{\dagger}_{i\mu\sigma}c_{p\sigma} + c^{\dagger}_{p\sigma}c_{i\mu\sigma}), \tag{2}$$

where $t_{p\mu}$ represent the hopping between *p*- and *μ*-orbitals, *l* and *r* represent the two transition-metal sites, *μ* is the *d*-orbital index (*μ* = *α*, *β*), $c^{\dagger}$ and *c* are the creation and annihilation operators, respectively.

Next, we identify the possible *p*–*d* hopping channels ($t_{p\mu}$) by following the interatomic Slater-Koster integrals[23]. Given that the ∠Cr–X/Y–Cr is close to 90° and only one *p*-orbital is considered in the superexchange path, the *d* electrons in one Cr ion can only reach the other Cr via the e_g-*p*-t_{2g} hopping channel (Fig. 3a). While for the *d* electrons from the same orbital couple with each other via the t_{2g}-*p*-t_{2g} or the e_g-*p*-e_g hopping channel, there is no way that two consecutive hopping processes are possible, see Fig. 3b,c. Taking into consideration the t_{2g} and e_g orbitals being of the half occupied and the empty e_g orbital, respectively, the exchange coupling mediated by the e_g-*p*-t_{2g} hopping channel is FM, and the AFM is forbidened by Pauli principle.

As shown in Fig. 3d, there are two fourth-order processes for the case of FM order on transition-metal cations: first with two electrons jumping away from the *p*-orbital of anion to e_g- and t_{2g}-orbitals, and two electrons coming back (i.e. the hopping process I and II); second with one electron from *p*-orbital hopping to e_g-orbital on one side, then the electron from t_{2g}-robital on the other side hopping to *p*-orbital, and two electrons coming back (i.e. the hopping process I and III). Then, the effective Hamiltonian for FM order is (for the details of derivation see the Supplementary materials)

$$H_{\mathrm{FM}} \approx -\frac{2t_1^2}{\Delta_1} - \frac{2t_2^2}{U_d+\Delta_2} - 2\left(\frac{t_1t_2}{\Delta_1} + \frac{t_1t_2}{U_d+\Delta_2}\right)^2 \frac{1}{U_d+\Delta_1+\Delta_2} - 2\left(\frac{t_1t_2}{\Delta_1}\right)^2 \frac{1}{\Delta_{\mathrm{CF}}}, \tag{3}$$

where $\Delta_1 = \varepsilon_{e_g\uparrow}$-$\varepsilon_{p\uparrow}$ (the energy difference between e_g- and *p*-orbitals), $\Delta_2 = \varepsilon_{t_{2g}\downarrow}$-$\varepsilon_{p\downarrow}$ (the energy difference between t_{2g}- and *p*-orbitals) and $\Delta_{\mathrm{CF}} = \varepsilon_{e_g\uparrow}$-$\varepsilon_{t_{2g}\uparrow}$ (the energy difference between e_g- and t_{2g}-orbitals due to the crystal field (CF)), t_1 and t_2 represent the hopping between *p*- and e_g-orbitals and *p*- and t_{2g}-orbitals, respectively, and U_d is the Coulomb repulsion between two electrons in *d*-orbital.

In the case of AFM only second-order processes are possible (i.e. the hopping process I or II). And the effective Hamiltonian for AFM order is

$$H_{\mathrm{AFM}} \approx -\frac{2t_1^2}{\Delta_1} - \frac{2t_2^2}{U_d+\Delta_2}. \tag{4}$$

According to $H_{ex} = H_{\mathrm{FM}}$ - $H_{\mathrm{AFM}} = -JS_1S_2$ (for Cr^{3+}, $S_1 = S_2 = 3/2$), we arrive at

$$J_1^{ex} = \frac{8}{9}(t_1t_2)^2\left[\left(\frac{1}{\Delta_1} + \frac{1}{U_d+\Delta_2}\right)^2 \frac{1}{U_d+\Delta_1+\Delta_2} + \frac{1}{\Delta_1^2\Delta_{\mathrm{CF}}}\right]. \tag{5}$$

Since the energy difference terms (Δ_1, Δ_2, and Δ_{CF}) are larger than 0, the J_1^{ex} is positive, i.e., the superexchange is FM ordering, which is in line with our analysis of exchange polarization. The corresponding parameters of Δ and *t* can be further extracted by projecting the Kohn–Sham states on the atomic Wannier functions of Cr-3*d* and X/Y-*p* orbitals[24]. Compared with the minior changes of $(t_1t_2)^2$ as substituting the anion (X/Y) by the heavier congener (see Supplementary Table 3), there are sizable reductions of Δ_1, Δ_2 and Δ_{CF} in the denominator of Eq. (5) [Fig. 4a, b], playing a decisive

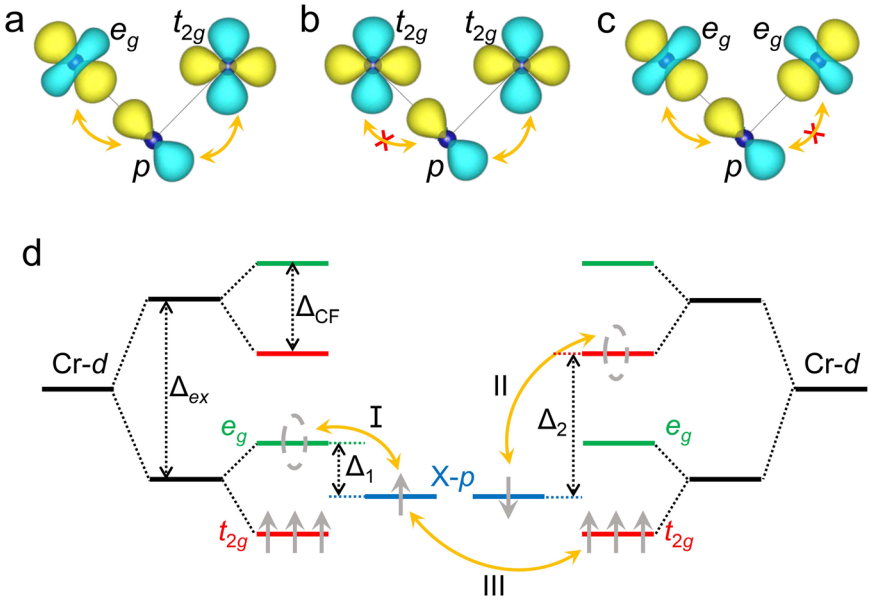

Fig. 3 Ferromagnetic superexchange mechanism. Superexchange channels between two cations via an intermediate anion: (**a**) e_g-p-t_{2g}, (**b**) t_{2g}-p-t_{2g} and (**c**) e_g-p-e_g. **d** Schematic diagrams of orbital evolution and superexchange interaction. Red and green bars represent t_{2g}- and e_g-orbitals, respectively. Δ_1, Δ_2 and Δ_{CF} are the energy difference between e_g- and p-orbitals, t_{2g}- and p-orbitals and e_g- and t_{2g}-orbitals, respectively. Process I, II and III represent the electron hopping between $p_\uparrow$- and $e_{g\uparrow}$-orbitals, $p_\downarrow$- and $t_{2g\downarrow}$-orbitals and $p_\uparrow$- and $t_{2g\uparrow}$-orbitals, respectively. Δ_{ex} is the exchange splits for Cr-d orbitals.

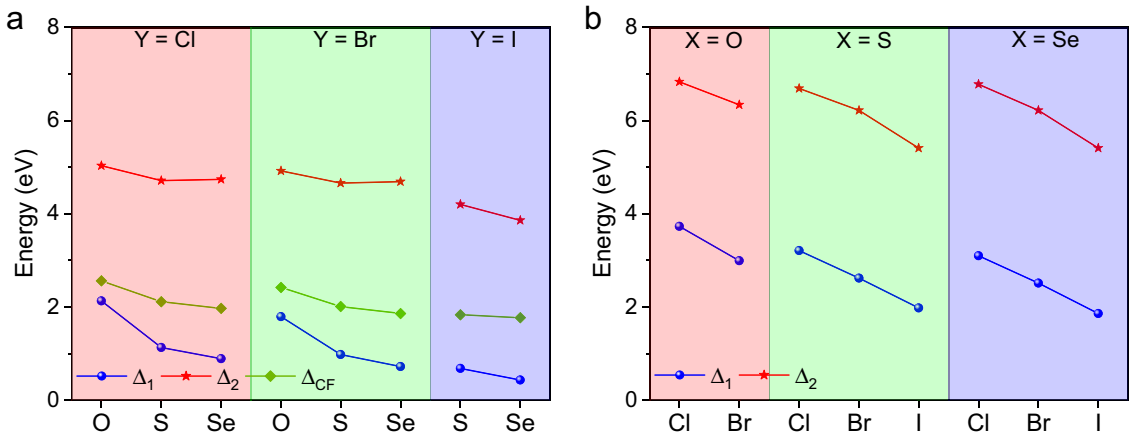

Fig. 4 Energy difference between different orbitals. Energy difference between e_g- and p-orbitals (Δ_1), t_{2g}- and p-orbitals (Δ_2) and e_g- and t_{2g}-orbitals (Δ_3) for (**a**) different chalcogen (X) and (**b**) halogen atoms (Y).

role in determining the strength of FM exchange interaction. Particularly, as replacing O by S (Se), the Δ_1 changes from around 2 eV to around (less than) 1 eV, which accounts for the great enhancement of J_1^{ex}. Moreover, because the Δ_1 and Δ_2 of X atom are less than those of Y atom, we conclude that the super-exchange path of Cr–X–Cr plays a major contribution to the spin coupling.

Given the smallest magnitude of Δ_1 among the energy difference terms in the denominator (Figs. 3d, 4), we quantitatively investigate the evolution of J_1^{ex} as a function of Δ_1 with the onsite Coulomb repulsion $U_d = 5$ eV and the hopping integrals $t_1 = t_2 =$ -0.5 eV. As shown in Fig. 5, J_1^{ex} increases significantly as decreasing Δ_1. However, when Δ_1 is around 1 eV, the corresponding J_1^{ex} reaches almost 30 meV, which is larger than that obtained from the DFT calculation (~11 meV). This discrepancy can be attributed to neglecting the interorbital Coulomb repulsion (U_d^{Inter}) when the e_g and t_{2g} orbitals are occupied at the same time, leading to the Δ_1 in Eq. 5 being replaced by an effective $\Delta_1^{eff} \sim \Delta_1 + U_d^{Inter}$. Thus, if we consider $\Delta_1 > 1$ eV, e.g. in the range of [1.5, 3.5], the corresponding J_1^{ex} obtained from this model are in good agreement with the calculated results (inset in Fig. 5), indicating the rationality and validity of this mode. Besides, by plotting the differential charge density of the CrOCl, CrSCl and CrSeCl monolayers in Fig. 6, we can identify that the electronic density in CrSCl and CrSeCl is large in the interstitial region between Cr and S/Se ion, implying the increased covalent contribution in the Cr–S/Se bond with respect to that in Cr–O bond, which is a synergy of the variation in t and Δ. It should be also noticed that substituting Cl by the late halogen elements gives rise to relatively weak changes in the covalent character of Cr–Y bonds (see Supplementary Fig. 6b), yielding a limited effect on tuning the J_1^{ex}.

Estimation of curie temperature

To determine the exact Curie temperature (T_c) in CrXY monolayers, we perform Monte Carlo simulations with the Metropolis algorithm based on the fully anisotropic Heisenberg model by

mcsolver package[25], using a $32 \times 32 \times 1$ matrix, the Hamiltonian reads

$$H = -J_1^{ex} \sum_{i,j} S_i S_j - J_2^{ex} \sum_{i,k} S_i S_k - J_3^{ex} \sum_{j,k} S_j S_k, \quad (6)$$

where spins are treated as classical vectors that can rotate and point to any space orientations. The Curie temperature can be accurately extracted from the peak of the specific heat capacity for the CrOCl and CrOBr monolayers as shown in Fig. 7a. In order to verify the reliability of this method, we have calculated the T_c of the CrI_3 monolayer by taking the magnetic exchange parameters J_1^{ex} and J_2^{ex} from refs. [26–28], and our results are in good agreement with those references (see Supplementary Table S4). From the Fig. 7b, the predicted Curie temperatures of CrSY and CrSeY monolayers approach or exceed the room temperature, owing to the larger J_1^{ex}. And T_c can be further enhanced under approximate tensile strains, 10% tensile stress can further raise the T_c of the CrSeI monolayer to 409 K.

In summary, we discover a series of the 2D FM semiconductor CrXY (X = O, S, Se; Y = Cl, Br, I) in $CrCl_2$ structure. Our study shows that the FM coupling is due to the hybridization between the empty e_g-orbital of Cr atoms and the p-orbital of anions under the three-fold rotational symmetry. This mechanism allows for the strategy of strengthening the FM coupling by increasing the covalent hybridization contribution of the Cr–X bond in CrXY. As we unveiled in the CrSY and CrSeY monolayers, utilizing this strategy the T_c could be greatly enhanced to room temperature. This high T_c renders these CrXY monolayers feasible candidates for 2D ferromagnetic materials and spintronic devices.

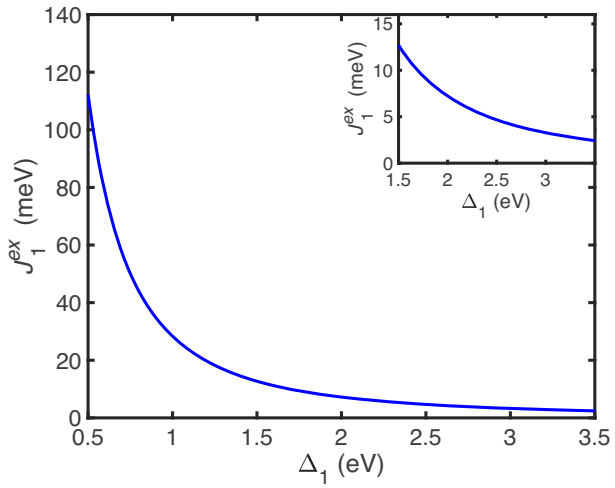

Fig. 5 Evolution of J_1^{ex} as a function of Δ_1 with $\Delta_2 = 5$ eV, $\Delta_{CF} = 2.5$ eV, $U_d = 5$ eV.

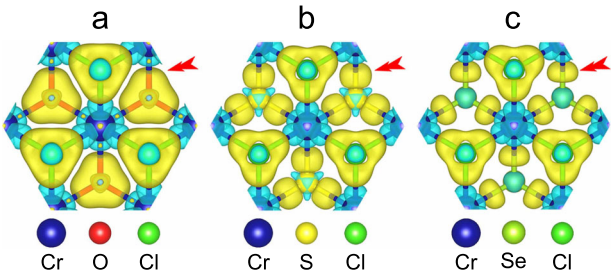

Fig. 6 Differential charge density of CrXCl monolayers. Differential charge density of (**a**) CrOCl, (**b**) CrSCl and (**c**) CrSeCl monolayers, where yellow and cyan regions denote charge accumulation and depletion with the isosurface being set to 0.06 e/Å^3. The red arrow indicates the electron in the center of the Cr–X bond.

METHODS

First-principles calculations

The spin-polarized first-principles calculations have been performed based on the projector augmented wave (PAW) pseudopotentials[29] implemented in the Vienna ab initio simulation package (VASP)[30,31]. The generalized gradient approximation in the Perdew–Burke–Ernzerh form[32,33] is used for treating the exchange-correlation effect, and the GGA + U method[34] is employed to properly describe the strong electron correlation effect of the Cr-3d orbitals ($U = 3.0$ eV)[35–37]. A cutoff energy of 500 eV is adopted for the plane wave expansion. The convergence criteria of geometrical optimization are 10^{-5} eV and 0.01 eV Å^{-1} for energy and force, respectively. For electronic self-consistent calculations, the energy and force convergence criteria are further decreased to 10^{-7} eV and 0.001 eV Å^{-1}, respectively. To avoid interactions between two periodic units, a vacuum space of 15 Å is employed. A Monkhorst-Pack k-point mesh of $10 \times 10 \times 1$ and $15 \times 15 \times 1$ are utilized to the structural optimization and the calculation of the electronic and magnetic properties for the unit cells, respectively. The phonon dispersion is calculated using a $4 \times 4 \times 1$ supercell with the finite displacement method by the PHONOPY software[38,39]. To investigate the thermal stability, we carry out isobaric-isothermal (NPT) ensemble molecular dynamics (MD) simulation at 300 K with the total simulation time of 20 ps and a time step of 2 fs by using Forcite code[40].

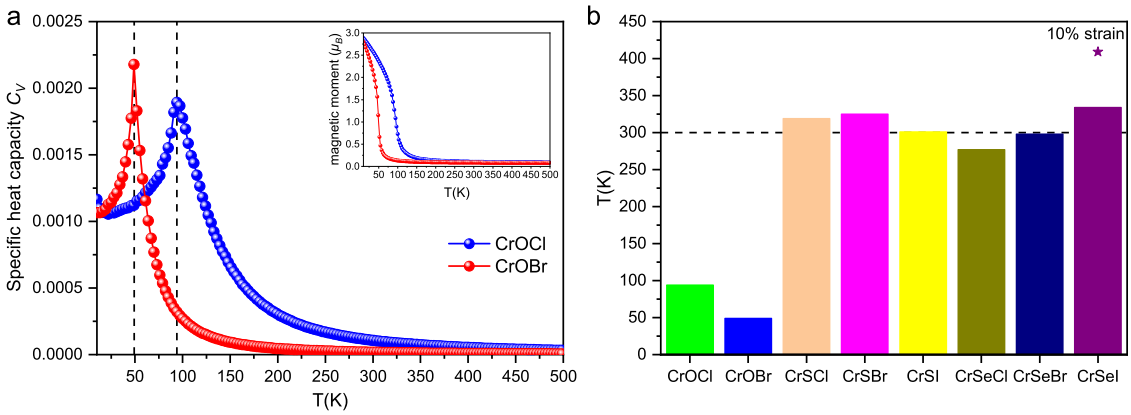

Fig. 7 Specific heat capacity and Curie temperature of CrXY monolayers. a Evolution of the Monte Carlo specific heat capacity of the CrOCl and CrOBr monolayers, the inset in (**a**) is the magnetic moment with the change of the temperature. **b** Curie temperature (T_c) in CrXY monolayers.

DATA AVAILABILITY

The data supporting the findings of this study are available within this article and its Supplementary Information. Additional data that support the findings of this study are available from the corresponding author on reasonable request.

Received: 23 October 2022; Accepted: 28 March 2023;
Published online: 08 April 2023

REFERENCES

1. Huang, B. et al. Layer-dependent ferromagnetism in a van der Waals crystal down to the monolayer limit. *Nature* **546**, 270–273 (2017).
2. Wolf, S. A. et al. Spintronics: a spin-based electronics vision for the future. *Science* **294**, 1488–1495 (2001).
3. Žutić, I., Fabian, J. & Sarma, S. D. Spintronics: fundamentals and applications. *Rev. Mod. Phys.* **76**, 323 (2004).
4. Fert, A. Nobel lecture: origin, development, and future of spintronics. *Rev. Mod. Phys.* **80**, 1517 (2008).
5. Gong, C. et al. Discovery of intrinsic ferromagnetism in two-dimensional van der waals crystals. *Nature* **546**, 265–269 (2017).
6. Miao, N. H., Xu, B., Zhu, L. G., Zhou, J. & Sun, Z. M. 2D intrinsic ferromagnets from van der Waals antiferromagnets. *J. Am. Chem. Soc.* **140**, 2417–2420 (2018).
7. Xiao, T. T., Wang, G. & Liao, Y. Theoretical prediction of two-dimensional CrOF sheet as a ferromagnetic semiconductor or a half-metal. *Chem. Phys.* **513**, 182–187 (2018).
8. Jiao, J. Y. et al. 2D Magnetic Janus semiconductors with exotic structural and quantum-phase transitions. *J. Phys. Chem. Lett.* **10**, 3922–3928 (2019).
9. Kabiraj, A., Kumar, M. & Mahapatra, S. High-throughput discovery of high Curie point two-dimensional ferromagnetic materials. *J. Phys. Chem. Lett.* **6**, 35 (2020).
10. Muhammad, I., Ali, A., Zhou, L. G., Zhang, W. & Wong, P. K. J. Vacancy-engineered half-metallicity and magnetic anisotropy in CrSI semiconductor monolayer. *J. Phys. Chem. Lett.* **909**, 164797 (2022).
11. Anderson, P. W. New approach to the theory of superexchange interactions. *Phys. Rev.* **115**, 2 (1959).
12. Anderson, P. W. Theory of magnetic exchange interactions: exchange in insulators and semiconductors. *Solid State Phys* **14**, 99–214 (1963).
13. Anderson, P. W., *A Career in Theoretical Physics* 113–130 (World Scientific, 1994).
14. Goodenough, J. B. An interpretation of the magnetic properties of the perovskite-type mixed crystals $La_{1-x}Sr_xCoO_{3-\lambda}$. *J. Phys. Chem. Solids* **6**, 287–297 (1958).
15. Kanamori, J. Superexchange interaction and symmetry properties of electron orbitals. *J. Phys. Chem. Solids* **10**, 87–98 (1959).
16. Sawatzky, G. A., Geertsma, W. & Haas, C. Magnetic interactions and covalency effects in mainly ionic compounds. *J. Magn. Magn. Mater.* **3**, 37–45 (1976).
17. Wang, J. H., Yip, S., Phillpot, S. R. & Wolf, D. Crystal instabilities at finite strain. *Phys. Rev. Lett.* **71**, 4182 (1993).
18. Ni, J. Y. et al. Giant biquadratic exchange in 2D magnets and its role in stabilizing ferromagnetism of $NiCl_2$ monolayers. *Phys. Rev. Lett.* **127**, 247204 (2021).
19. Sandratskii, L. M. Noncollinear magnetism in itinerant-electron systems: theory and applications. *Adv. Phys.* **47**, 91–160 (1998).
20. Mermin, N. D. & Wagner, H. Absence of ferromagnetism or antiferromagnetism in one- or two-dimensional isotropic heisenberg models. *Phys. Rev. Lett.* **17**, 1133 (1966).
21. Xiang, H. J., Lee, C., Koo, H. J., Gong, X. G. & Whangbo, M. H. Magnetic properties and energy-mapping analysis. *Dalton Trans.* **42**, 823–853 (2013).
22. Šabani, D., Bacaksiz, C. & Milošević, M. V. Ab initio methodology for magnetic exchange parameters: generic four-state energy mapping onto a Heisenberg spin Hamiltonian. *Phys. Rev. B* **102**, 014457 (2020).
23. Slater, J. C. & Koster, G. F. Simplified LCAO method for the periodic potential problem. *Phys. Rev* **94**, 1498 (1954).
24. Pizzi, G. et al. Wannier90 as a community code: new features and applications. *J. Phys. Condens. Matter* **32**, 165902 (2020).
25. Liu, L. et al. Magnetic switches via electric field in BN nanoribbons. *Appl. Surf. Sci.* **480**, 300–307 (2019).
26. Lu, X. B., Fei, R. X. & Yang, L. Curie temperature of emerging two-dimensional magnetic structures. *Phys. Rev. B* **100**, 205409 (2019).
27. Rehman, M. U. et al. Quantum anomalous Hall effect by coupling heavy atomic layers with CrI_3. *Phys. Rev. B* **100**, 195422 (2019).
28. Webster, L. & Yan, J. A. Strain-tunable magnetic anisotropy in monolayer $CrCl_3$, $CrBr_3$, and CrI_3. *Phys. Rev. B* **98**, 144411 (2018).
29. Blöchl, P. E. Projector augmented-wave method. *Phys. Rev. B* **50**, 17953 (1994).
30. Kresse, G. & Furthmller, J. Efficient iterative schemes for ab initio total-energy calculations using a plane-wave basis set. *Phys. Rev. B* **54**, 11169 (1996).
31. Kresse, G. & Joubert, D. From ultrasoft pseudopotentials to the projector augmented-wave method. *Phys. Rev. B* **59**, 1758 (1999).
32. Perdew, J. P. et al. Atoms, molecules, solids, and surfaces: Applications of the generalized gradient approximation for exchange and correlation. *Phys. Rev. B* **46**, 6671 (1993).
33. Perdew, J. P. & Wang, Y. Accurate and simple analytic representation of the electron-gas correlation energy. *Phys. Rev. B* **45**, 13244 (1992).
34. Dudarev, S. L., Botton, G. A., Savrasov, S. Y., Humphreys, C. J. & Sutton, A. P. Electron-energy-loss spectra and the structural stability of nickel oxide: an LSDA + *U* study. *Phys. Rev. B* **57**, 1505 (1998).
35. Solovyev, L. V., Dederichs, P. H. & Anisimov, V. I. Corrected atomic limit in the local-density approximation and the electronic structure of *d* impurities in Rb. *Phys. Rev. B* **50**, 16861 (1994).
36. Wang, L., Maxisch, T. & Ceder, G. Oxidation energies of transition metal oxides within the GGA + *U* framework. *Phys. Rev. B* **73**, 195107 (2006).
37. Huang, C. X. et al. Toward intrinsic room-temperature ferromagnetism in two-dimensional semiconductors. *J. Am. Chem. Soc.* **140**, 11519–11525 (2018).
38. Gonze, X. & Lee, C. Dynamical matrices, Born effective charges, dielectric permittivity tensors, and interatomic force constants from density-functional perturbation theory. *Phys. Rev. B* **55**, 10355 (1997).
39. Togo, A., Oba, F. & Tanaka, I. First-principles calculations of the ferroelastic transition between rutile-type and $CaCl_2$-type SiO_2 at high pressures. *Phys. Rev. B* **78**, 134106 (2008).
40. Rappe, A. K., Casewit, C. J., Colwell, K. S., Goddard III, W. A. & Skiff, W. M. Uff, a full periodic table force field for molecular mechanics and molecular dynamics simulations. *J. Am. Chem. Soc.* **114**, 10024–10035 (1992).

ACKNOWLEDGEMENTS

The research is supported by the Science Challenge Project (Grant No. TZ2016003-1-105), the Tianjin Natural Science Fundation (Grant No. 20JCZDJC00750), and the Fundamental Research Funds for the Central Universities, Nankai University (Grant Nos. 63211107 and 63201182)

AUTHOR CONTRIBUTIONS

H.-R.Z. performed the DFT calculations, compiled the figures and wrote the manuscript. H.-R.Z., B.S. and X.Z. conceived and analyzed Hamiltonian model. B.S. and X.Z. proposed and supervised the manuscript. All authors contributed to the analysis and discussion of the results.

COMPETING INTERESTS

The authors declare no competing interests.

ADDITIONAL INFORMATION

Supplementary information The online version contains supplementary material available at https://doi.org/10.1038/s41524-023-01013-8.

Correspondence and requests for materials should be addressed to Bin Shao or Xu Zuo.

Reprints and permission information is available at http://www.nature.com/reprints

Publisher's note Springer Nature remains neutral with regard to jurisdictional claims in published maps and institutional affiliations.